HHS Public Access

Author manuscript

Stat Med. Author manuscript; available in PMC 2016 July 25.

Published in final edited form as:

Stat Med. 2016 May 20; 35(11): 1848–1865. doi:10.1002/sim.6785.

Bayesian Penalized Spline Models for the Analysis of Spatio-Temporal Count Data

Cici Bauer[a,*], **Jon Wakefield**[b], **Håvard Rue**[c], **Steve Self**[d], **Zijian Feng**[e], and **Yu Wang**[e]

[a]Department of Biostatistics, Brown University

[b]Department of Statistics, University of Washington

[c]Norwegian University of Science and Technology

[d]Fred Hutchinson Cancer Research Center

[e]Chinese Center for Disease Control and Prevention

Abstract

In recent years, the availability of infectious disease counts in time and space has increased, and consequently there has been renewed interest in model formulation for such data. In this paper, we describe a model that was motivated by the need to analyze hand, foot and mouth disease (HFMD) surveillance data in China. The data are aggregated by geographical areas and by week, with the aims of the analysis being to gain insight into the space-time dynamics and to make short-term prediction to implement public health campaigns in those areas with a large predicted disease burden. The model we develop decomposes disease risk into marginal spatial and temporal components, and a space-time interaction piece. The latter is the crucial element, and we use a tensor product spline model with a Markov random field prior on the coefficients of the basis functions. The model can be formulated as a Gaussian Markov random field and so fast computation can be carried out using the integrated nested Laplace approximation (INLA) approach. A simulation study shows that the model can pick up complex space-time structure and our analysis of HFMD data in the central north region of China provides new insights into the dynamics of the disease.

Keywords

Bayesian spatio-temporal analysis; Gaussian Markov random field; INLA; infectious diseases; penalized splines; surveillance count data

1. Introduction

In recent years, the modeling of infectious disease data in space and time has gained increasing popularity. The aims of such modeling are many fold but gaining insights into space-time dynamics, which may give etiological insights, is a common objective. Modeling may also allow one to predict the potential effects of health interventions such as the

*Correspondence to: Department of Biostatistics, Brown University. Cici_Bauer@brown.edu.

introduction of vaccination. Many examples of such infectious disease data arise from government disease surveillance systems, and in many situations are in the form of spatially and temporally aggregated disease counts. In this paper, the motivating example was hand, foot and mouth disease (HFMD) surveillance data collected and monitored by the Chinese Center for Disease Control and Prevention. The dataset comprises weekly number of HFMD cases in 341 prefectures between 2009 and 2010. In this paper we develop a Bayesian space-time modeling framework for infectious disease count data, and achieve significant computational savings using the integrated nested Laplace approximation (INLA) technique. The goals of such modeling are to utilize the surveillance data to understand the space-time dynamics of the infectious disease outbreaks, and to provide predictions of future disease counts to aid in policy formation.

The literature on space-time models is ample, with many proposals based on disease mapping models. For example, in (1) and (2) the risk evolution over time is assumed to take a parametric form. A different approach is taken by (3) and (4), where the risks for every time period are modeled as time-independent spatial random effects with a time-specific precision parameter for the spatial variability. In the context of modeling multiple diseases, (5) proposes a temporally independent multivariate conditional autoregressive (MCAR) model for lung cancer mortality, with data on both males and females being studied. In (6), the authors propose a shared compartment model where the underlying risk for each disease is separated into a shared and a disease-specific component. Many of these space-time models were developed for non-infectious diseases such as cancers.

Disease mapping models developed for non-infectious diseases have been used, often for descriptive purposes, for infectious disease data, see for example, (7) for flu and (8) for meningococcal disease. In a series of papers (9; 10; 11; 12) a framework for the analysis of infectious disease surveillance counts has been developed. In its simplest form, the models can be viewed as Poisson branching process models with immigration, with mean risk being decomposed into an endemic component and an epidemic component. These models have been applied to a variety of diseases and have also used vaccination coverage as a covariate (13; 14). (15) modeled weekly counts of HFMD in prefectures of China using a similar negative binomial model with epidemic and endemic components. In a different approach, time series susceptible-infected-recovered (SIR) models have been developed (16; 17). The fitting of SIR models (and their variants) is challenging unless the populations under consideration are small, however, since the number of individuals in each of the compartments is imputed under the above Bayesian approach to inference (18). A variety of alternative approaches have been suggested for situations in which populations are not small, but all are computationally expensive (19; 20). Approximate Bayesian Computation (ABC) methods have been proposed as an alternative (21; 22).

In recent years, spline models have become increasingly popular in the space-time disease mapping setting, see for example (23). However, such models have mostly been applied to provide a flexible way of modeling the temporal trend, see for example (24). A notable exception is (25) who describes a broader class of regression spline models with spatial-temporal relative risks being modeled as spatially varying or randomly varying regression B-splines. (26) and (27) both consider space-time splines models, though do not include

Markov random field (MRF) prior penalty terms, which is the cornerstone of the approach we describe in this paper. (28) compares a traditional space-time conditional autoregressive (CAR) model and a CAR-Pspline model in the context of small area predictions, with inference made using penalized quasi-likelihood (PQL).

In this paper, the approach we take to modeling the space-time spread of infectious disease data is to decompose the relative risk of disease into three components: a large-scale temporal trend, a large-scale spatial trend and a space-time interaction. The latter is the crucial element, and we use a tensor product B-spline model with a Markov random field (MRF) prior on the coefficients of the basis function. Such a model formulation allows the computation to be carried out using the integrated nested Laplace approximation (INLA) technique, resulting in significant computational savings when compared to a classical MCMC approach. Our approach therefore has the advantage of fast computation and easy implementation using `R` and existing packages.

The outline of this paper is as follows. We begin with a motivating example that concerns the China hand-foot-mouth (HFMD) surveillance data in Section 2. In Section 3 we describe the Bayesian spatial-temporal models that we propose. In Section 4, we demonstrate the performance of our proposed models via a simulation study. The simulated data is designed to mimic the epidemic center movements in space and time typically observed in infectious disease surveillance data. We return to the HFMD data in Section 5 and describe the results after applying the models to the dataset. We conclude the paper with a discussion in Section 6. The supplementary materials contain more technical details and additional supporting information.

2. Motivating Example

In this section, we provide details of the China HFMD surveillance data analyzed in this paper. HFMD is an acute contagious viral infection that has caused large-scale outbreaks in Asia during the past decade (29). It is caused by enterovirus pathogens and usually involves mild or moderate symptoms such as fever, oral ulcer or rashes on the hand and foot. HFMD is a disease often seen in children and in a small fraction of cases there is severe illness with neurological problems, and even death. Little is known about the etiology of the enterovirus, the factors associated with its spread, or an effective means of public health intervention. Therefore understanding the dynamics of HFMD patterns of spread can greatly benefit authorities charged with policy making to control this infectious disease.

Enterovirus-related HFMD, with the first large-scale epidemic outbreak in 2008 in China, has been included as one of the 39 notifiable infectious diseases in the Chinese Center for Disease Control and Prevention (CCDC) disease surveillance system. Each reported case from the CCDC surveillance system includes information on the person’s current home address, gender, age and the symptom onset date. Therefore, the disease surveillance system from China provides an extensive data resource for space-time modeling. More information about these data can be found in (15).

In this paper, we analyze data from the central north region of China from 2009 and 2010; this region is shown in relation to the whole of China in the supplementary materials. The central north region consists of 59 prefectures spread in five provinces and one direct-controlled municipality (i.e., Tianjin, Hebei, Henan, Shandong, Shanxi and Beijing). The total population in the region is estimated to be 318,022,505 in 2009/2010. Within the region, 418,949 and 478,238 HFMD cases were reported in 2009 and 2010, respectively. Here we aggregate the number of HFMD cases by week and by prefecture, see Figure 1(a). The temporal trend is clear: the epidemic starts around March, reaches its peak in May/June and gradually dies down towards the winter. This is the same pattern observed in both years, though the time that the epidemic reaches its peak seems to be later in 2010 than in 2009.

Based on the population composition in each prefecture, we calculate weekly expected numbers of counts adjusting for age (with age bands 0–0.9, 1–2.9, 3–5.9, 6–9.9 and ≥10 years) and gender, using internal standardization (30). These expected numbers are shown in Figure 1(b), with a wide range from 18 to 364.We then calculate the marginal standardized morbidity ratios (SMRs) across time. These SMRs are the ratios of the total counts to the expected counts (adjusted for the confounders age and gender) over 2009–2010. A thematic map of the resulting SMRs is presented in Figure 1(c). Though subject to sampling variability, the spatial variation in the SMR is clearly seen in the map (an animation of the weekly log SMRs can be found at http://www.stat.brown.edu/cbauer/). However, the temporal pattern in the SMRs is unclear apart from a general south-to-north movement of the area with high SMRs. These initial examinations clearly suggest a model with spatial and temporal components is needed for analyzing the China HFMD data.

3. Methods

In this section, we describe the Bayesian spatial-temporal models that we propose. We start by describing the overall model framework, followed by details on each of the model components.

3.1. The Poisson Likelihood

Let Y_{it} denote the observed disease counts and E_{it} the expected counts, which account for the known confounders such as age and gender, in area i and in week t, $i = 1, \ldots, I$; $t = 1, \ldots, T$. In the HFMD example, the population is treated as constant at each time point so that $E_{it} = E_i$. The constant population is based on the assumption that the changes in population size over time are relatively small and so can be ignored. The expected count E_i is calculated using internal standardization, which takes into account of the differences in age-gender populations between areas.

The data model is a Poisson distribution with relative risk μ_{it}

$$Y_{\mathrm{it}}|\mu_{\mathrm{it}} \sim \mathrm{Poisson}(E_i \mu_{\mathrm{it}}). \quad (1)$$

Our overall strategy is to decompose the relative risk into the following components

$$\log(\mu_{\mathrm{it}})=\alpha+\boldsymbol{z}_{\mathrm{it}}^{T}\boldsymbol{\beta}+f_{\mathrm{S}}(\boldsymbol{x}_i)+f_{\mathrm{T}}(t)+f_{\mathrm{ST}}(\boldsymbol{x}_i,t) \quad (2)$$

where α is the intercept, $\boldsymbol{z}_{it}$ is a vector of area-level covariates, and $\boldsymbol{x}_i = (x_{1i}, x_{2i})$ is the centroid of area i. In this formulation, $f_S(\boldsymbol{x}_i)$ is the spatial trend, $f_T(t)$ is the temporal trend and $f_{ST}(\boldsymbol{x}_i, t)$ is the spatial-temporal interaction. In a Bayesian framework, the spatial and temporal dependency is incorporated into the model through the prior. We now describe the priors used for the spatial trend, the temporal trend, and the spatial-temporal interaction in (2) respectively.

3.1.1. Temporal trend—The temporal component is modeled as the sum of a large-scale component, and noise terms with and without temporal structure

$$f_{\mathrm{T}}(t)=\boldsymbol{x}_t^{T}\boldsymbol{\delta}+\varepsilon_t+\gamma_t.$$

The large-scale component $\boldsymbol{x}_t^{T}\boldsymbol{\delta}$ can be modeled using parametric or semi-parametric models, which we have assumed can be represented via a linear basis. A popular example of the latter are spline models, see (24) and (25). As an alternative, seasonal variability in the data can be modeled via frequency domain models. For example, we can include a set of harmonic functions

$$\boldsymbol{x}_t^{T}\boldsymbol{\delta}=\sum_{s=1}^{S}[a_s\ \sin(\omega_s t)+b_s\ \cos(\omega_s t)],\quad s=1,\ldots,T/2 \quad (3)$$

where S is the number of harmonics, $\boldsymbol{\delta} = \{a_s, b_s, s = 1, \ldots, S\}$ and ω_s are the Fourier frequencies with $\omega_s = 2\pi s/52$ for weekly data. The row vector $\boldsymbol{x}_t$ is of length $2S$ with the sth pair of entries consisting of $[\sin(\omega_s t), \cos(\omega_s t)]$. The unstructured temporal term may be modeled as $\varepsilon_t \sim_{iid} \mathrm{N}(0, \tau_\varepsilon^{-1})$ while γ_t, which picks up short-term temporal structure, may be given a conditional autoregressive prior. In this paper we use a second-order random walk prior denoted as RW2. This model is a local stochastic smoothing model and may be represented as

$$p(\boldsymbol{\gamma}|\tau_\gamma) \propto \exp\left[-\frac{\tau_\gamma}{2}\boldsymbol{\gamma}^{\mathrm{T}}\boldsymbol{A}_{\mathrm{T}}\boldsymbol{\gamma}\right],$$

where the $T \times T$ matrix $\boldsymbol{A}_{\mathrm{T}}$ is of rank $T - 2$ and has the form

$$\boldsymbol{A}_{\mathrm{T}}=\begin{bmatrix} 1 & -2 & 1 & & & & & & \\ -2 & 5 & -4 & 1 & & & & & \\ 1 & -4 & 6 & -4 & 1 & & & & \\ & 1 & -4 & 6 & -4 & 1 & & & \\ & & \ddots & \ddots & \ddots & \ddots & \ddots & & \\ & & & 1 & -4 & 6 & -4 & 1 & \\ & & & & 1 & -4 & 6 & -4 & 1 \\ & & & & & 1 & -4 & 5 & -2 \\ & & & & & & 1 & -2 & 1 \end{bmatrix}, \quad (4)$$

with the blank spaces corresponding to zeros. We use τ through out the paper for the precision parameter, which is the inverse of the variance. The subscript of τ indicates the random variable with which the precision parameter is associated. Further technical details on this model, including the conditional mean and variance, are provided in the supplementary materials.

3.1.2. Spatial trend—The spatial trend is modeled as

$$f_{\mathrm{S}}(\boldsymbol{x}_i)=\beta_1 x_{1i}+\beta_2 x_{2i}+\upsilon_i+u_i. \quad (5)$$

The covariates x_{1i} and x_{2i} represent the latitude and longitude of the centroid of area i and β_1 and β_2 are the associated coefficients. The unstructured spatial terms υ_i is assigned a $\mathrm{N}(0,\tau_\upsilon^{-1})$ prior, and the structured spatial term u_i is assigned an intrinsic conditional autoregressive (ICAR) prior. Hence, we are using the classic (31) convolution model. The joint distribution of the structured spatial term u_i is

$$\pi(\boldsymbol{u}|\tau_u) \propto \exp\left[-\frac{1}{2}\boldsymbol{u}^{\mathrm{T}}\boldsymbol{A}_{\mathrm{S}}\boldsymbol{u}\right], \quad (6)$$

where $\boldsymbol{A}_{\mathrm{S}}$ has entries

$$A_{S_{ij}}=\begin{cases} m_i & i=j, \\ -1 & i\sim j, \\ 0 & \text{otherwise}, \end{cases} \quad (7)$$

with $i \sim j$ indicating that areas i and j are neighbors defined as areas sharing the same boundary, and m_i the number of neighbors for area i. Further details of the ICAR model are relegated to the supplementary materials.

3.1.3. Spatial-temporal interaction—Models with only spatial and temporal trends are usually insufficient for modeling the variation in temporal dynamics between regions, particularly for infectious diseases. Hence, the spatial-temporal interaction term we define is

crucial, as this term captures the space-time dynamics of the infectious disease spread. In a disease mapping context, for example, (32) and (33), it has been suggested that a space-time interaction term could be constructed by combining the spatial random effects $\boldsymbol{u}$ and the temporal random effects $\boldsymbol{\gamma}$. However, such a form contains a large number of random effects, IT to be exact, which is not a parsimonious representation. In addition, the interaction term adds great complexity to the model and makes the implementation for Bayesian inference, usually via Markov chain Monte Carlo (MCMC), very difficult for data with many areas and/or time points.

Motivated by (33), we propose an alternative approach to constructing the interaction term. We model the space-time interaction surface with a bivariate spline, and place a GMRF prior on the coefficients associated with the basis functions. Specifically, we assume

$$f_{\mathrm{ST}}(\boldsymbol{x}_i, t) = \sum_{k=1}^{K} b_{kt} B_{ik}, \quad k = 1, \ldots, K, \tag{8}$$

where B_{ik} is a tensor product of two univariate cubic B-spline functions, one in each spatial dimension, so that B_{ik} is a function of $\boldsymbol{x}_i$. For notational convenience we index the bivariate basis functions by k. The number of basis functions K will typically be far less than the number of areas I, and so the number of latent random effects is reduced. Because these basis functions are constructed as a tensor product, they can be visualized as being laid out on a rectangular grid. Figure 2(b) presents such visualization using a simulated data set, for a total of 36 basis functions (6 for each spatial coordinate). The advantages of choosing a cubic B-spline include the computation efficiency and the relative insensitivity to the choice of basis numbers and locations (34; 35). More details of the tensor product basis functions can be found in the supplementary materials.

The spatial-temporal structure of the interaction is imposed through the prior on the basis coefficients and can take one of the following four types, as with the disease mapping approach of (33)

Type I: A product of independent normal priors so that there is no spatial or temporal structure in the spline coefficients

$$\pi(\boldsymbol{b}|\tau_b) \propto \exp\left[-\frac{\tau_b}{2}\sum_{k=1}^{K}\sum_{t=1}^{T} b_{kt}^2\right].$$

This type of interaction assumes that, after accounting for spatial and temporal main effects, the residuals do not have structure in space and time. This model is the easiest to implement but the least appealing in a biological sense.

Type II: A second-order random walk (RW2) prior on the temporal structure with no spatial structure, so that we have a product of K temporal smoothing priors

$$\pi(\boldsymbol{b}|\tau_b) \propto \exp\left[-\frac{\tau_b}{2}\sum_{k=1}^{K}\sum_{t=3}^{T}(b_{kt} - 2b_{k,t-1} + b_{k,t-2})^2\right].$$

Hence, the interactions have temporal structure but the bases are independent across space.

Type III: An ICAR prior in space but with no temporal structure, so that we have a product of T independent spatial models

$$\pi(\boldsymbol{b}|\tau_b) \propto \exp\left[-\frac{\tau_b}{2}\sum_{t=1}^{T}\sum_{k\sim k'}(b_{kt} - b_{k't})^2\right].$$

The notation $k \sim k'$ indicates that bases k and k' are first order neighbors, hence each interior basis has four neighbors. This model assumes that at time t, the bases that are close to each other are more likely to be similar, but across time the T sets are independent.

Type IV: A Kronecker product of RW2 and ICAR priors

$$\pi(\boldsymbol{b}|\tau_b) \propto \exp\left[-\frac{\tau_b}{2}\sum_{t=3}^{T}\sum_{k\sim k'}\{(b_{kt} - 2b_{k,t-1} + b_{k,t-2}) - (b_{k't} - 2b_{k',t-1} + b_{k',t-2})\}^2\right].$$

This model assumes that the basis coefficient b_{kt} at location $\boldsymbol{x}_k$ and at time t depends on those from the two previous time periods $b_{k,t-1}$ and $b_{k,t-2}$, as well as those from the neighboring basis $\boldsymbol{x}_{k'}$, $k' \sim k$. In addition, b_{kt} depends on those coefficients in the neighboring bases in the two previous time points, i.e. $b_{k',t-1}$ and $b_{k',t-2}$, for $k' \sim k$. Therefore estimation of the coefficients borrows information in both space and time.

In addition to reducing the dimension of random effects, our proposed method has the advantage that, even with complicated structures, after writing $(b_{11}, \ldots, b_{K1}, b_{12}, \ldots, b_{K2}, \ldots, b_{1T}, \ldots, b_{KT})'$ as $\boldsymbol{b}$, all four types of interactions have a unified representation as GMRF models with the general form

$$\pi(\boldsymbol{b}|\tau_b) \propto \exp\left[-\frac{\tau_b}{2}\boldsymbol{b}^{\mathrm{T}}\boldsymbol{A}_{\mathrm{ST}}\boldsymbol{b}\right].$$

The structure matrix $\boldsymbol{A}_{\mathrm{ST}}$ of the spline coefficients is then the Kronecker product of the structure matrix for the space $\boldsymbol{A}_{\mathrm{S}}$ and the temporal structure matrix $\boldsymbol{A}_{\mathrm{T}}$, i.e. $\boldsymbol{A}_{\mathrm{ST}} = \boldsymbol{A}_{\mathrm{S}} \otimes \boldsymbol{A}_{\mathrm{T}}$. The supplementary materials give details on the form of $\boldsymbol{A}_{\mathrm{ST}}$ for each interaction model. Such a representation also brings a flexibility to the modeling, as one can select different spatial and temporal structures, depending on the application.

One other advantage of our proposed models is in the computation. The GMRFs presentation of the spatial-temporal dynamics makes the computation far more convenient. In particular, this model can be fitted using the fast and flexible integrated nested Laplace

approximation (INLA) technique (36). INLA has been demonstrated to provide accurate inference in a number of applications (36; 37; 38; 39; 40) and, compared to the more traditional MCMC method, is orders of magnitude faster for the model described above. In the supplementary materials we provide the `WinBUGS` code to implement our proposed models using MCMC, as well as the code that uses the `R` package `INLA`. We also show in the supplementary materials a numerical comparison between MCMC and INLA.

4. Simulation Study

4.1. Data Generation

In this section we describe a simulation study to investigate the performance of our proposed models. The key novelty of our proposed models lies upon the spatial-temporal interaction so we focus on assessing this aspect and fit the Poisson model (1), with the relative risk

$$\log(\mu_{\mathrm{it}})=\alpha+f_{\mathrm{ST}}(\boldsymbol{x}_i,t), \quad (9)$$

where f_{ST} is described by (8).

The study region is a unit square and we select two equal-distance inner knots in each spatial dimension to construct the tensor product cubic B-splines bases, so that $K = 6^2 = 36$.We assume $T = 24$ discrete observation times. The simulation is constructed to mimic the movements of epidemic centers over time. We first obtain fixed values of the spline basis coefficients b_{kt}, using gamma functions and one sine function of time t, and then use these b_{kt} to construct the underlying risk surface. The functions for obtaining the values of b_{kt} are treated as unknown at the analysis. Figure 2(a) plots these coefficients versus time with the curves being color coded by their locations, which are shown in panel (b). The values of the coefficients are chosen so that higher values are given to those in the bottom left corner at early weeks of the observation period, those in the top left corner at middle weeks, and those in the top right corner at later weeks. We choose the expected number of cases E_i to be between 5 and 50 and assume they are constant over the study period. The observed counts Y_{it} are then simulated at $I = 150$ randomly selected locations, which are indicated by the points in Figure 2(b). These point locations are used to represent areal centroids. The MRF prior is with respect to the bases, and so for the interaction term this is the only place that requires specification of a neighborhood structure. The simulated weekly counts Y_{it} range from 0 to 1063. In Figures 2(c) and (d) the number of cases over space and time are displayed. The aggregated counts in panel (c) show large spatial variation, ranging from 2148 to 9541. The weekly observed counts aggregated over space in panel (d) show two peaks, which is similar to that observed in the China HFMD data. The supplementary materials include more details on the simulation, such as the map of the realized E_i, and the bubble plots of the simulated number of cases at selected time points which give more details on how epidemic centers move over time.

4.2. Results of the simulation study

We fit the spatial-temporal interaction model (9) with the four interaction priors described in Section 3.1.3. A Gamma(1, 0.98) distribution is used as the prior for the precision parameter τ_b. Results of the parameter estimates are given in the supplementary materials, along with a sensitivity analysis with different priors for the precision parameter. Time series plots of the estimated basis coefficients are shown in Figure 3, with one for each interaction type. The true values of the coefficients are superimposed in the graph using the color scheme of Figure 2, and the grey lines denote the posterior median estimates. In the Type I interaction model where the coefficients have no spatial or temporal structure, the grey lines are very jagged and substantially deviate from the truth. In the Type II model where a RW2 model is used for the temporal structure in the interaction, the estimated coefficients are much smoother over time and closer to the truth. In the Type III model, the estimates are similar to those observed in the Type I model. Because the majority of the variation in the simulated data is temporal, smoothing across space alone cannot improve the estimation greatly. Finally, the Type IV model improves on the Type III fit and provides the estimates that are the closest to the true values. We now assess the model fits more formally.

The overall measure of the model fit may be assessed using the conditional predictive ordinate (CPO) (41; 42) which represents a particular form of cross-validation measure. The CPO of observation it is

$$\mathrm{CPO}_{\mathrm{it}} = \int \Pr(y_{\mathrm{it}} | \boldsymbol{y}_{-\mathrm{it}}, \boldsymbol{\theta}) \pi(\boldsymbol{\theta} | \boldsymbol{y}_{-\mathrm{it}}) d\boldsymbol{\theta}$$

where $\boldsymbol{y}_{-it}$ represent the data with observation y_{it} removed. We may calculate $\sum_{i=1}^{I} \sum_{t=1}^{T} \log \mathrm{CPO}_{\mathrm{it}}$ and models with larger values are preferred. (43) discuss how CPO values may be calculated efficiently with INLA, without the need to fit the model $I \times T$ times. For the simulated data, the sum of the log CPO values under the four types of interactions (scaled by the maximum, which is the Type II model) are: −429, 0, −106 and −20. The CPO values from the Type II and IV models are considerably higher than those from the Type I and III models, so that the former are preferred to the latter, which is not surprising given the strong temporal structure in the data.

Examining the change of the spline coefficients provides some knowledge of the temporal trend in the risk. However, we would also like to obtain the estimated log relative risks at the observed locations. We select four areas with different expected numbers (E = 5, 15, 30, 50) and examine the model fits. In Figure 4(a) we give the true log relative risk for these four areas while in panel (b), we plot the log SMRs. It is clear that areas with lower expected numbers have larger variability in the log SMRs. In panels (c)–(f) we show the fits from the four types of interaction models. In these plots the estimated log relative risks using our models are clearly more accurate than the log SMRs. Informally comparing the four types of interaction models using these figures, the fits from the Type II and IV interaction models are closest to the truth.

Finally we examine the prediction performance of our proposed models. We take the data until time $T^\star$ and predict the number of cases within q week ahead, i.e., y_{it} for $t = T^\star + 1, \ldots, T^* + q$. The prediction performance is evaluated using the mean squared error of prediction (MSEP) given by

$$\mathrm{MSEP} = \frac{1}{Iq} \sum_{T^\star+1}^{T^*+q} \sum_{i=1}^{I} (\hat{y}_{\mathrm{it}} - y_{\mathrm{it}})^2. \quad (10)$$

The results for $q = 1$ and $q = 2$, i.e. predicting 1 and 2 time periods ahead, are given in Table 1. We choose $T^* = 6$ to give a minimum that has sufficient observed data for prediction. For each $T^\star$ and q, the MSEP is reported for the Type I–IV models, with the smallest MSEP indicated in bold. Type II model predominately outperform the other types by giving the smaller MSEP, with 15 out of 18 weeks for $q = 1$ and 11 out of 17 weeks for $q = 2$. The Type IV model gives the smallest MSEP in all other weeks for $q = 1$ and three of the remaining weeks for $q = 2$. The predictions become worse for all models in weeks 19–22, which is the period in which the second epidemic peak occurs. This is somewhat unsurprising: without additional information of the disease etiology or drivers of the outbreaks, prediction of the time when an epidemic "kicks off" is generally very difficult in infectious diseases, particularly based on the surveillance data alone. Nevertheless, when the surveillance data is the only source to understand the space-time dynamics of the infectious disease process, including the temporal component is more crucial than the spatial one, which is emphasized by the better performance of the Type II and Type IV models.

5. Application to HFMD Data in China

We now return to the HFMD data in the central north region of China over years 2009–2010. We assume the Poisson model (1) with μ_{it} given by (2). The study region is rescaled to a [0, 1] × [0, 1] square but retain the ratio $[\max(x_{i2}) - \min(x_{i2})]/[\max(x_{i1}) - \min(x_{i1})]$. We include the population density per square kilometer as a covariate, denoted as z_i, with this variable being normalized to have mean 0 and standard deviation 1. We manually remove those basis functions that lie outside of the study region. The locations of $K = 16$ bases used in the analysis are shown in Figure 1(d).

The model is implemented using INLA, and parameter point and interval estimates are presented in Table 2. The running time for the four models are 307, 501, 289 and 429 seconds, respectively, on a MacBook Pro with 2.6 GHz Intel Core i7 processor. In the Type I and III models, we find that population density has a significant positive association, which is consistent with the fecal-oral transmission route of HFMD since areas in which children are in closer proximity are likely to have greater rates of infection. Estimates of the structured and unstructured temporal components γ_t and ε_t are very similar in the four models, and therefore we only show the results from the Type IV interaction model in Figure 5. The overall temporal pattern that is common to all areas is captured in the structured temporal random effect $\boldsymbol{\gamma}$ and is shown in Figure 5(a). The unstructured temporal random effects ε_t, shown in Figure 5(b), reflects the residual temporal variability after accounting for the structured RW2 temporal effect γ_t. No clear pattern is observed and the range of the

estimated ε_t is narrow (between −0.10 and 0.075). The estimated structured spatial random effect u_i ranges from −0.067 to 0.085, and the unstructured spatial random effect υ_i ranges from −1.1 to 0.95 so that the latter dominates. Maps of the median estimates are shown in Figure 5(c) and (d). These random effects are log relative risks of disease and so the spatial terms are not of great epidemiological significance. The sum of the log CPO values, again scaled by the Type II model, are: −7672, 0, −8075 and −3894, strongly suggesting the Type II model is most appropriate for the HFMD data.

An animation of the term $\hat{\alpha}+\hat{\gamma}_t+\sum_{k=1}^{K}\hat{b}_{kt}B_{ik}$ can be found at http://www.stat.brown.edu/cbauer/, which provides insight into the broad-scale space-time dynamics of HFMD. Compared to the log SMR maps, the movement of the epidemic center is much clearer as the regions with elevated relative risks are easier to identify. We see two local epidemics that start, respectively, in the north and south-west areas around week 22, and gradually move towards each other. This movement is not evident in the log SMR maps.

Next we take the first $T^{\star}$ weeks of HFMD surveillance data and perform the q-week ahead prediction of total HFMD counts, by area. The performance of the prediction is again assessed via the MSEP in (10). For comparison the prediction is also carried out using the epidemic/endemic model of (9) implemented within the `R surveillance` package. Specifically, we use the form $y_{it}|\theta_{it} \sim$ Poisson(θ_{it}) with

$$\theta_{\mathrm{it}}=\lambda_i^{\mathrm{AR}}y_{i,t-1}+\lambda_i^{\mathrm{NE}}\sum_{j\neq i}w_{ji}y_{j,t-1}+E_i\lambda_{\mathrm{it}}^{\mathrm{EN}} \quad (11)$$

where $\lambda_i^{\mathrm{AR}}=\alpha_0^{\mathrm{AR}}+b_i^{\mathrm{AR}}$ represents the autoregressive "self-area" component with random effects b_i^{AR}, $\lambda_i^{\mathrm{NE}}=\alpha_0^{\mathrm{NE}}+b_i^{\mathrm{NE}}$ is an autoregressive "neighboring area" component (defined as sharing a common boundary) with random effects b_i^{AR}, and

$$\lambda_{it}^{\mathrm{EN}}=\alpha_0^{\mathrm{EN}}+b_i^{\mathrm{EN}}+\beta z_i+\sum_{s=1}^{S}\left(\gamma_s\ \sin\ \left[\frac{st}{52}2\pi\right]+\delta_s\ \sin\ \left[\frac{st}{52}2\pi\right]\right)$$

is an endemic component with the random effects b_i^{EN} and $S = 1$. All the random effects are assumed independently and normally distributed. Results with T^{*} starting at week 90 are presented in Table 3. More comprehensive experiments with T^{*} going back as early as week 34 can be found in the supplementary materials. We attempted analyses with T^{*} smaller than 34 but the epidemic/endemic model encountered convergence issues. Compared to the epidemic/endemic model, out of the 14 weeks our models give smaller MSEP in 8 weeks for $q = 1$ and 7 weeks for $q = 2$. Among the four types of interaction models, the Type II and IV models give smaller MSEP in all weeks. Adding spatial structure can aid the prediction, as seen in the smaller MSEP in the Type III model as compared to the Type I model. However, since most of the variation in the data comes from the temporal trend, it is the temporal structure components included in the Type II and IV models that are most important for prediction.

In addition to the q-week ahead prediction we also investigate the performance of our proposed models for cumulative prediction, where we take the first T^* weeks of the observations and predict the total HFMD counts for the remaining weeks in 2009 and 2010, by area. As can be seen in Table 4, in all weeks, our models give better prediction than epi/end model, except in the last week, where the scenario reverts to the 1-week ahead prediction. The results suggest that our proposed models perform as well as the epidemic/endemic model for short-term prediction, and outperform the competing model when prediction is carried out over longer time period.

Residuals plots of these models can be found in the supplementary materials. There is still considerable variation in the residuals from all models and some systematic variability showing that not all of the signal is being adequately modeled.

6. Discussion and Future Work

In this paper we have described a model for space-time infectious disease count data. The model bridges the gap between disease mapping models for chronic diseases and the more traditional SIR type models that are difficult to fit when the populations are large and individual-level information such as time of infection is not available. A number of aspects deserve further discussion.

The choice of prior distributions on the random effects variances in the interaction models is challenging because of the conditional interpretation, which changes across the four model types. An obvious approach is to use simulation, in tandem with substantive knowledge on the range of relative risks. For example, we may believe that the 95% range of the residual relative risks is [0.1, 10], which means that the range of the spline contribution is $\sum_k b_{kt}B_{ik}$ is [log(0.1), log(10)]. Experimentation with different prior choices via simulation can be carried out to achieve this aim. This is the approach that was taken to set the priors in our analysis, and the details can be found in the supplementary materials. From a practical point of view, our approach is computationally efficient since it is based on INLA. The improvement in computation time when compared with MCMC is considerable.

For the China central north HFMD data our model has allowed the following insights. In each year the epidemic moves from two centers, a major one in the south and a smaller one in the north. Population density is also seen to be an important aggregate level predictor, the credible intervals for the Type I and III models do not contain zero, but the intervals of the Type II and IV models contain zero, because the more flexible temporal model has absorbed some of the association with population density. This highlights the differences between models for prediction and those with which the identification of important covariates is sought. Without the etiology knowledge of the disease, prediction of future counts is difficult, in particular using the surveillance data alone. For HFMD disease, most of the variation in the surveillance data comes from the temporal trend. Hence, it is crucial to include the temporal structure in models for prediction.

The epidemic/endemic model is very appealing since it has autoregressive components, which allows aggregate level transmission to be estimated, and a good implementation. We

would not suggest that our model be used as a replacement. Rather, we think the approaches are complimentary. The model we have described has the appealing feature of producing a smoothly time-varying relative risk surface and this can greatly help in gaining insight into the space-time dynamics.

Supplementary Material

Refer to Web version on PubMed Central for supplementary material.

References

1. Bernardinelli L, Clayton D, Pascutto C, Montomoli C, Ghislandi M, Songini M. Bayesian analysis of space-time variation in disease risk. Statistics in Medicine. 1995; 14:2433–2443. [PubMed: 8711279]
2. Assunçaõ RM, Reis IA, Oliveira CD. Diffusion and prediction of Leishmaniasis in a large metropolitan area in Brazil with a Bayesian space-time model. Statistics in Medicine. 2001 Aug. 20:2319–2335. [PubMed: 11468766]
3. Waller LA, Carlin BP, Xia H, Gelfand AE. Hierarchical spatio-temporal mapping of disease rates. Journal of the American Statistical Association. 1997; 92:607–617.
4. Xia H, Carlin BP. Spatio-temporal models with errors in covariates: mapping Ohio lung cancer mortality. Statistics in Medicine. 1998; 17:2025–2043. [PubMed: 9789912]
5. Richardson S, Abellan JJ, Best N. Bayesian spatio-temporal analysis of joint patterns of male and female lung cancer risks in Yorkshire (UK). Statistical Methods in Medical Research. 2006; 15(4): 385–407. [PubMed: 16886738]
6. Knorr-Held L, Best N. A shared component model for detecting joint and selective clustering of two diseases. Journal of the Royal Statistical Society. Series A (Statistics in Society). 2001; 164(1):73–85. URL http://www.jstor.org/stable/2680535.
7. Mugglin A, Cressie N, Gemmell I. Hierarchical statistical modelling of influenza epidemic dynamics in space and time. Statistics in Medicine. 2002; 21:2703–2721. [PubMed: 12228886]
8. Knorr-Held L, Richardson S. A Hierarchical model for space-time surveillance data on meningococcal disease incidence. Journal of the Royal Statistical Society: Series C (Applied Statistics). 2003; 52:169–183.
9. Held L, Hohle M, Hofmann M. A statistical framework for the analysis of multivariate infectious disease surveillance counts. Statistical Modelling. 2005; 5:187–199.
10. Paul M, Held L, Toschke AM. Multivariate modelling of infectious disease surveillance data. Statistics in Medicine. 2008; 27:6250–6267. [PubMed: 18800337]
11. Paul M, Held L. Predictive assessment of a non-linear random effects model for multivariate time series of infectious disease counts. Statistics in Medicine. 2011; 30:1118–1136. [PubMed: 21484849]
12. Held L, Paul M. Modeling seasonality in space-time infectious disease surveillance data. Biometrical Journal. 2012; 54:824–843. [PubMed: 23034894]
13. Höhle M, Siedler A, Bader HM, Ludwig M, Heininger U, von Kries R. Assessment of varicella vaccine effectiveness in germany: a time-series approach. Epidemiology and Infection. 2011; 139:1710–1719. [PubMed: 21156098]
14. Herzog S, Paul M, Held L. Heterogeneity in vaccination coverage explains the size and occurrence of measles epidemics in german surveillance data. Epidemiology and Infection. 2011; 139:505–515. [PubMed: 20619079]
15. Wang Y, Feng Z, Yang Y, Self S, Gao Y, Longini I, Wakefield J, Zhang J, Wang L, Chen X, et al. Hand, foot and mouth disease in china: patterns and spread and transmissibility. Epidemiology. 2011; 22:781–792. [PubMed: 21968769]
16. Xia Y, Bjørnstad ON, Grenfell B. Measles metapopulation dynamics: a gravity model for epidemiological coupling and dynamics. The American Naturalist. 2004; 164:267–281.

17. Jandarov R, Haran M, Bjørnstad O, Grenfell B. Emulating a gravity model to infer the spatiotemporal dynamics of an infectious disease. Journal of the Royal Statistical Society: Series C (Applied Statistics). 2014; 63(3):423–444.
18. O'Neill P, Roberts G. Bayesian inference for partially observed stochastic epidemics. Journal of the Royal Statistical Society, Series A. 1999; 162:121–129.
19. Cauchemez S, Ferguson N. Likelihood-based estimation of continuous-time epidemic models from time-series data: application to measles transmission in london. Journal of the Royal Society Interface. 2008; 5:885–897.
20. He D, Ionides E, King A. Plug-and-play inference for disease dynamics: measles in large and small populations as a case study. Journal of the Royal Society Interface. 2010; 7:271–283.
21. McKinley T, Cook A, Deardon R. Inference in epidemic models without likelihoods. The International Journal of Biostatistics. 2009; 5:24.
22. Toni T, Welch D, Strelkowa N, Ipsen A, Stumpf M. Approximate Bayesian computation scheme for parameter inference and model selection in dynamical systems. Journal of the Royal Society Interface. 2010; 6:187–202.
23. Kneib T, Fahrmeir L. Structured additive regression for categorical space-time data: A mixed model approach. Biometrics. 2006; 62:109–118. [PubMed: 16542236]
24. MacNab YC, Dean CB. Spatio-temporal modelling of rates for the construction of disease maps. Statistics in Medicine. 2002; 21:347–358. [PubMed: 11813222]
25. MacNab YC, Gustafson P. Regression B-spline smoothing in Bayesian disease mapping: with an application to patient safety surveillance. Statistics in Medicine. 2007; 26:4455–4474. [PubMed: 17357989]
26. Ugarte M, Goicoa T, Militino A. Spatio-temporal modeling of mortality risk using penalized splines. Environmetrics. 2010; 21:270–289.
27. Lee D, Durbán M. P-spline ANOVA-type interaction models for spatio-temporal smoothing. Statistical Modelling. 2011; 11:49–69.
28. Etxeberria J, Goicoa T, Ugarte MD, Militino AF. Evaluating space-time models for short-term cancer mortality risk predictions in small areas. Biometrical Journal. 2014; 56(3):383–402. [PubMed: 24301220]
29. Tong C, Bible J. Global epidemiology of enterovirus 71. Future Virology. 2009; 4:501–510.
30. Wakefield J. Disease mapping and spatial regression with count data. Biostatistics. 2007; 8:158–183. [PubMed: 16809429]
31. Besag J, York J, Mollié A. Bayesian image restoration with two applications in spatial statistics. Annals of the Institute of Statistics and Mathematics. 1991; 43:1–59.
32. Clayton, D. Generalized linear mixed models. In: Gilks, W.; Richardson, S.; Spiegelhalter, D., editors. Markov Chain Monte Carlo in Practice. Chapman and Hall; 1996. p. 275-301.
33. Knorr-Held L. Bayesian modelling of inseparable space-time variation in disease risk. Statistics in Medicine. 2000; 19:2555–2567. [PubMed: 10960871]
34. Ruppert D. Selecting the number of knots for penalized splines. Journal of computational and graphical statistics. 2002; 11(4)
35. MacNab YC. Spline smoothing in bayesian disease mapping. Environmetrics. 2007 Nov; 18(7): 727–744. doi:
36. Rue H, Martino S, Chopin N. Approximate Bayesian inference for latent Gaussian models using integrated nested Laplace approximations (with discussion). Journal of the Royal Statistical Society, Series B. 2009; 71:319–392.
37. Fong Y, Rue H, Wakefield J. Bayesian inference for generalized linear mixed models. Biostatistics. 2010; 11:397–412. [PubMed: 19966070]
38. Paul M, Riebler A, Bachmann L, Rue H, Held L. Bayesian bivariate meta-analysis of diagnostic test studies using integrated nested laplace approximations. Statistics in Medicine. 2010; 29:1325–1339. [PubMed: 20101670]
39. Schrodle B, Held L, Riebler A, Danuser J. Using inla for the evaluation of veterinary surveillance data from switzerland: A case study. Journal of the Royal Statistical Society, Series C. 2011; 60:261–279.

40. Riebler A, Held L, Rue H. Estimation and extrapolation of time trends in registry data – borrowing strength from related populations. Annals of Applied Statistics. 2012; 6:304–333.

41. Pettit L. The conditional predictive ordinate for the normal distribution. Journal of the Royal Statistical Society, Series B. 1990; 52:175–184.

42. Geisser, S. Predicitve Inference: An Introduction. London: Chapman and Hall; 1993.

43. Held, L.; Schrödle, B.; Rue, H. Posterior and cross-validatory predictive checks: A comparison of MCMC and INLA. In: Kneib, T.; Tutz, G., editors. Statistical Modeling and Regression Structures – Festschrift in Honour of Ludwig Fahrmeir. Physica-Verlag; 2010. p. 91-110.

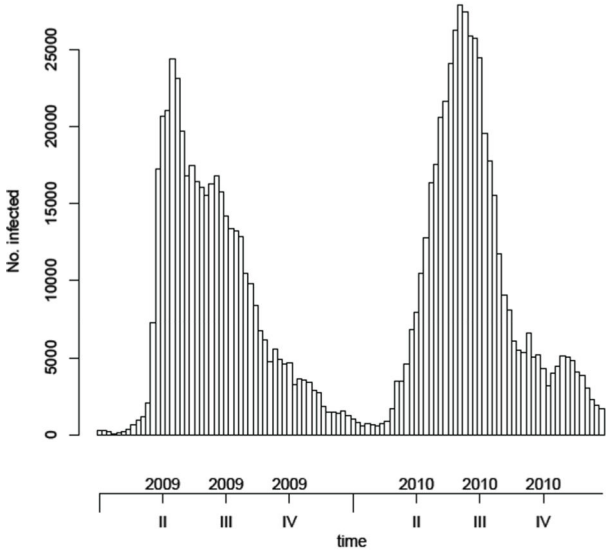

(a) weekly numbers of cases

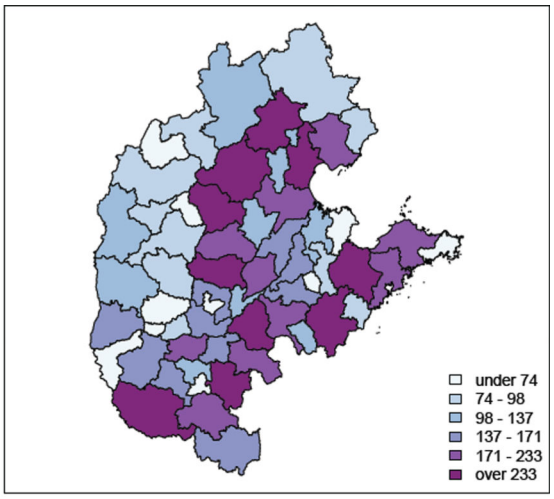

(b) weekly expected numbers

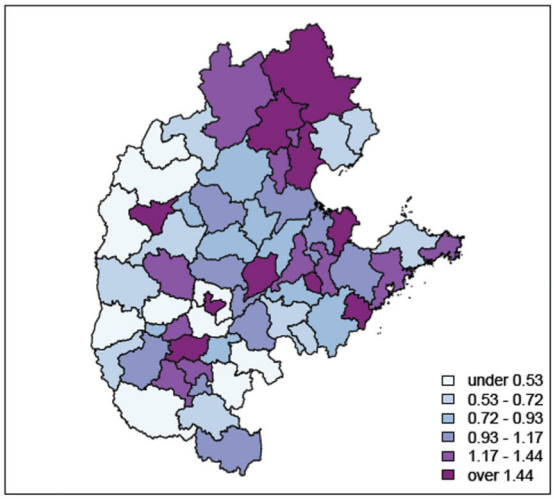

(c) marginal SMR

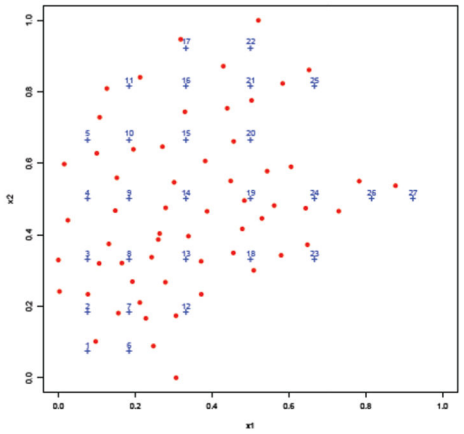

(d) location of prefectures and spline bases, after scaling.

Figure 1.

Summaries of the central north region of China HFMD data from 2009–2010: (a) weekly numbers of cases, (b) weekly expected numbers, (c) marginal (across time) SMR, (d) centroids of prefectures (red dots) and location of spline bases (blue crosses), after scaling the study region.

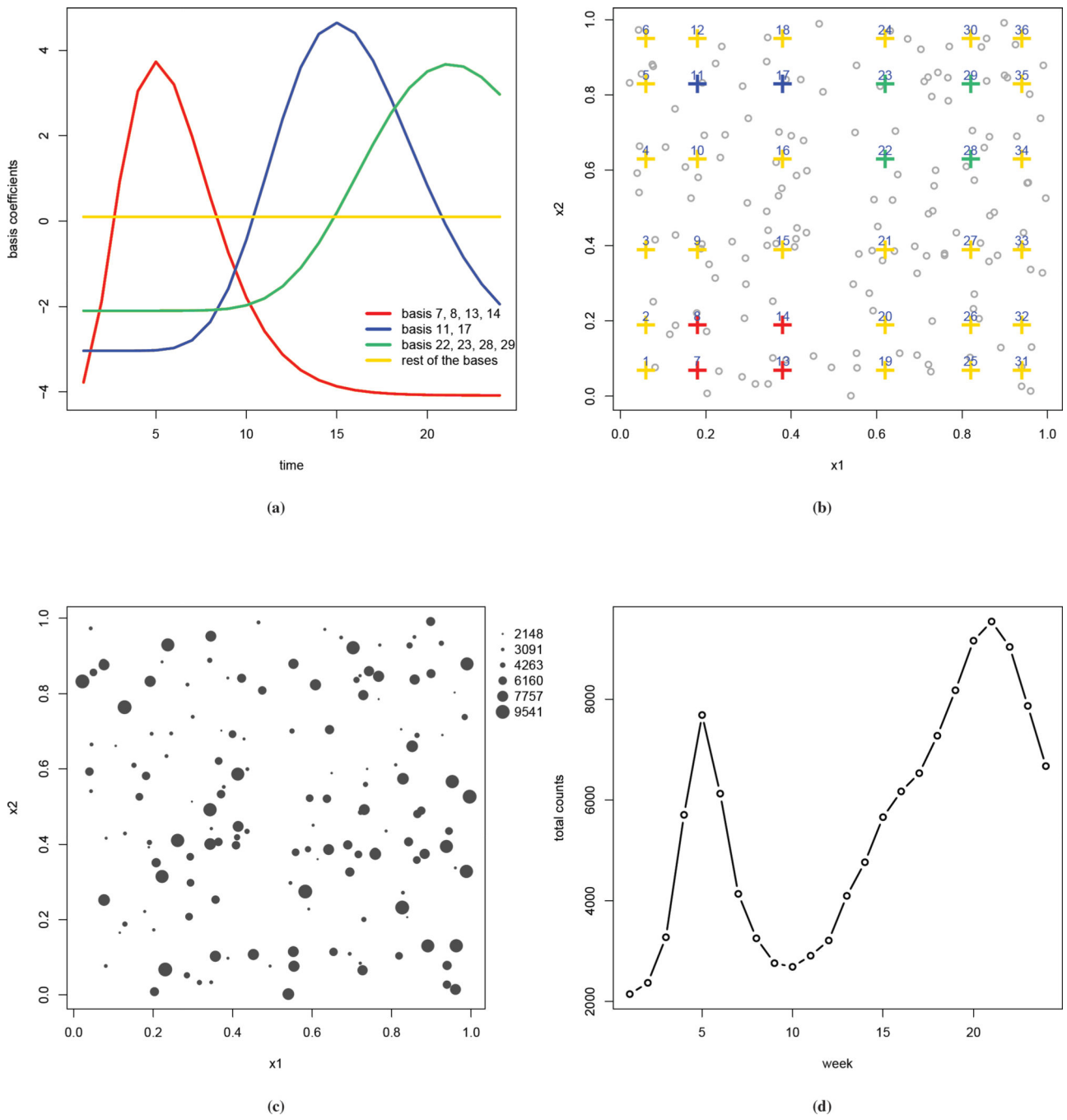

Figure 2.

Simulated Data: (a) true values of the basis functions b_{kt} versus time; (b) locations of the basis coefficients, color coded as in (a); the grey dots are the locations of the observed counts; (c) number of cases aggregated over time (with the size of the circles being proportional to the number of cases); (d) number of cases, aggregated over space, plotted by week.

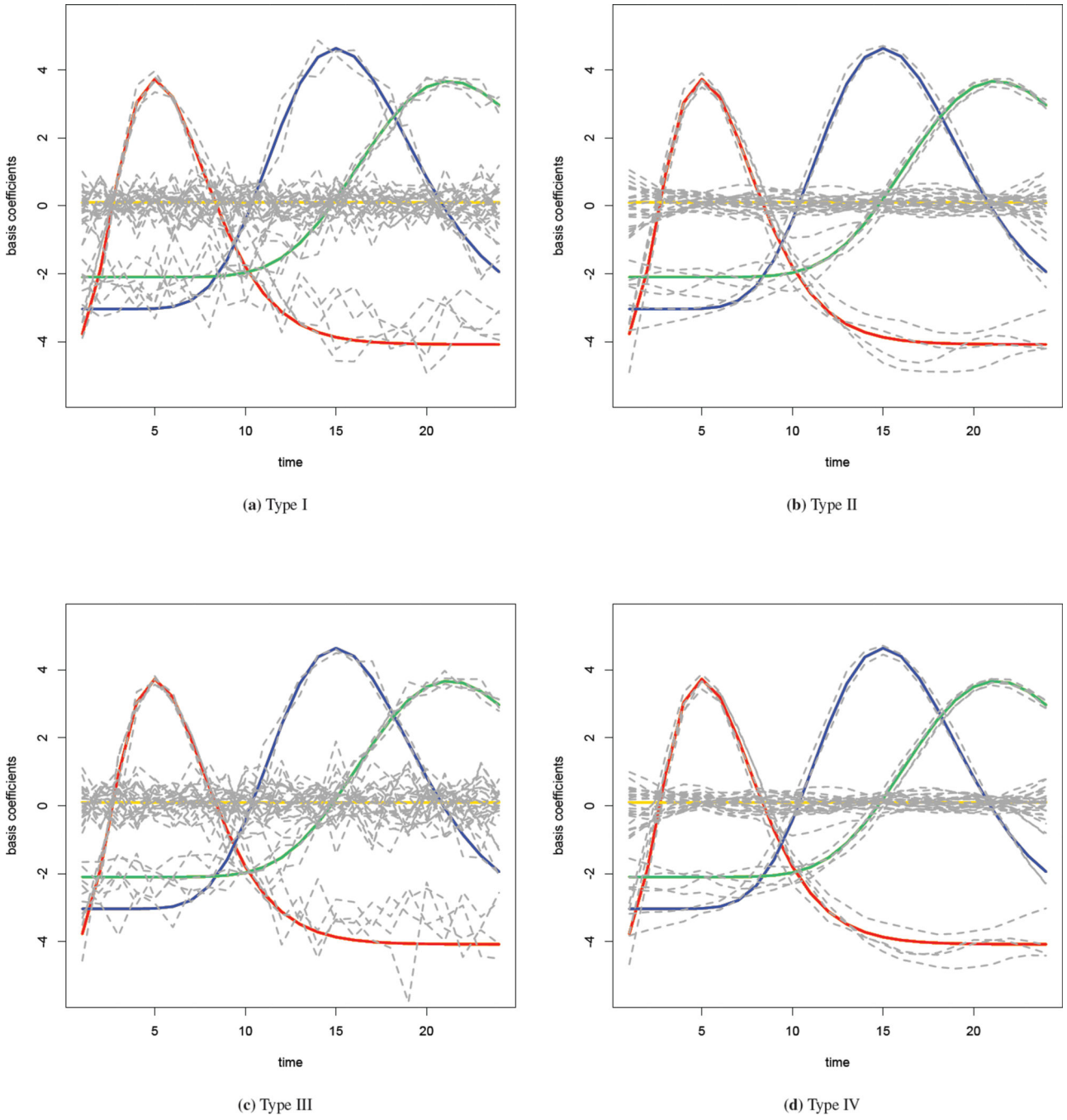

Figure 3.
Estimated basis coefficients with four different priors in the simulation study: true values are colored as in Figure 2, while the grey lines are the estimates.

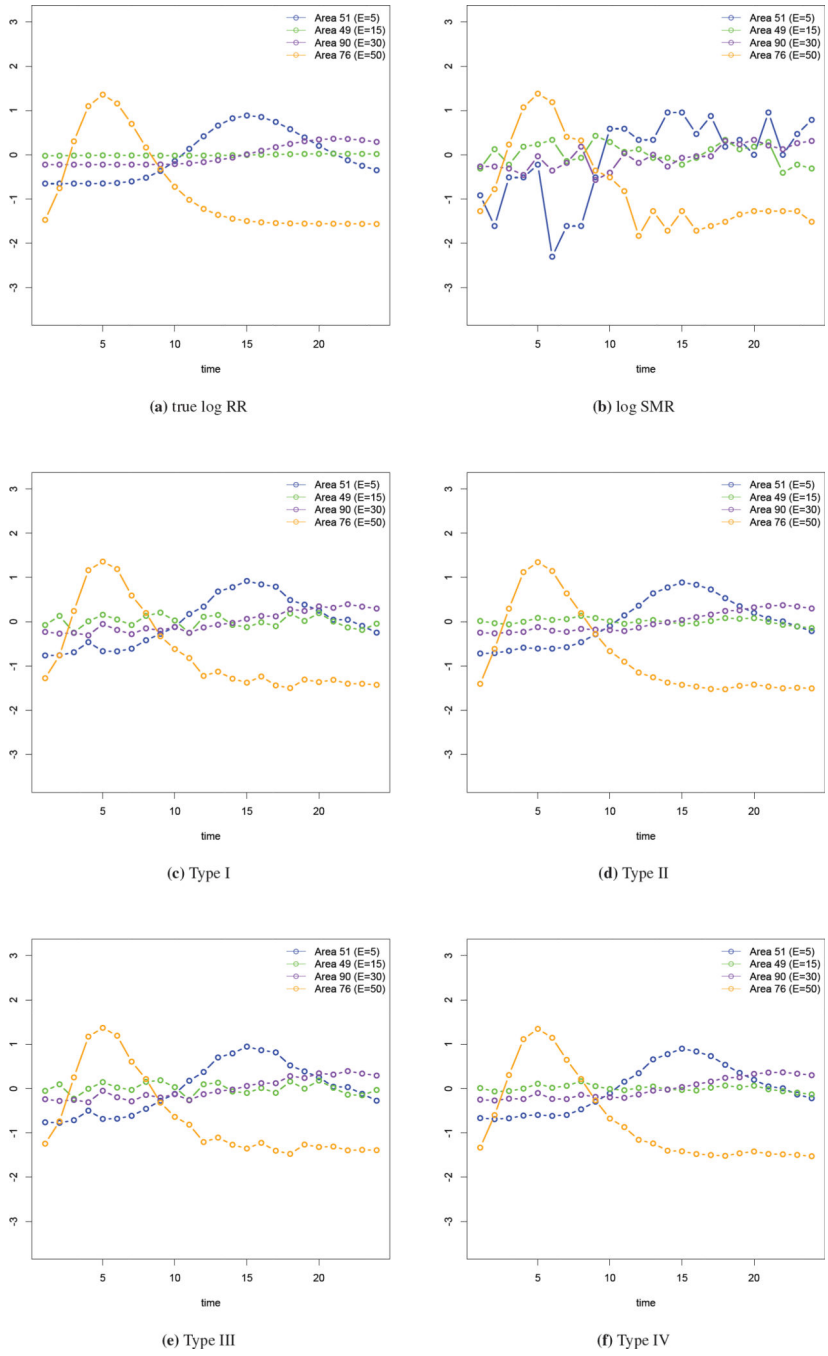

Figure 4.
Comparison of the log relative risk in four selected areas.

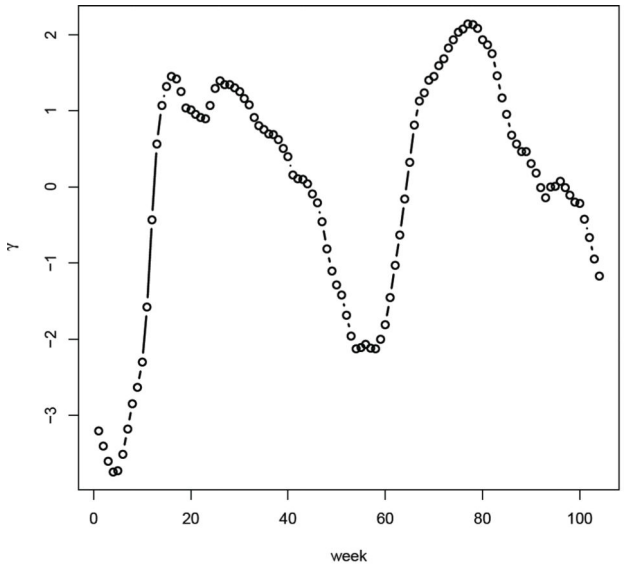

(a) structured time γ_t

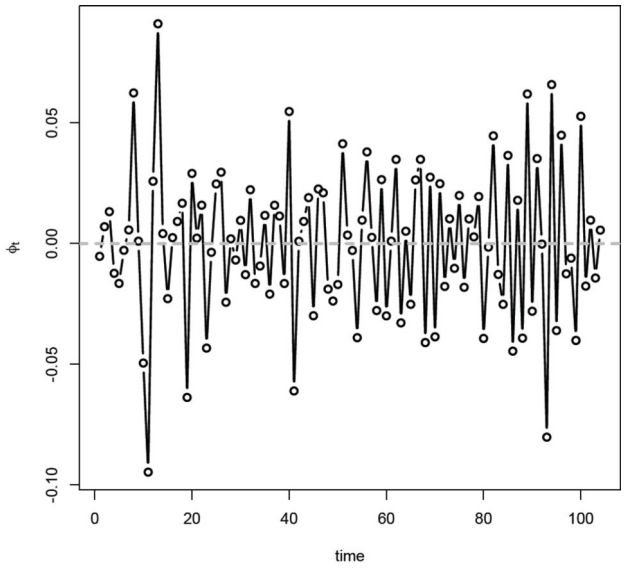

(b) unstructured time ϵ_t

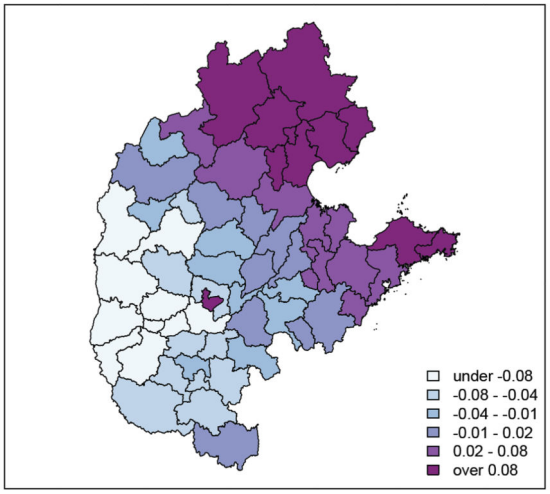

(c) structured spatial u_i

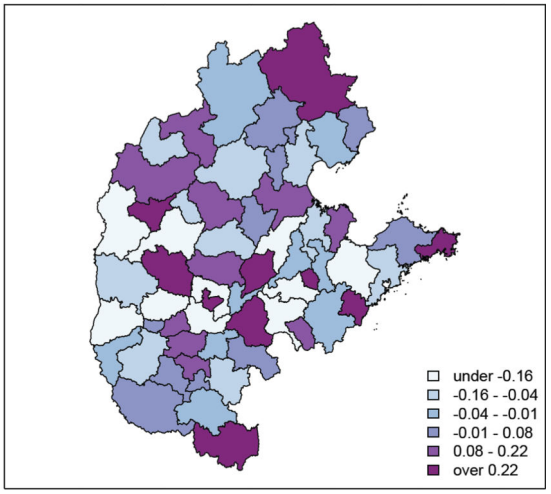

(d) unstructured spatial v_i

Figure 5.

Estimated temporal component γ and φ, and spatial component ***u*** and υ from the Type IV interaction model with the China central north HFMD data.

Table 1

The model is fitted to the simulated observations up until $T^{\star}$, and predictions are made for $q = 1$ and $q = 2$ weeks ahead. For each T^{*} and q, the mean squared error of prediction (MSEP) is reported for the Type I–IV models, with the smallest MSEP indicated in bold.

	$q = 1$				$q = 2$			
$T^{\star}$	Type I	Type II	Type III	Type IV	Type I	Type II	Type III	Type IV
6	857	**683**	911	687	**504**	804	527	819
7	153	**36**	142	43	135	**44**	107	67
8	115	**35**	73	45	128	**44**	83	61
9	135	**26**	90	39	134	**42**	96	64
10	134	**31**	100	46	197	**45**	173	67
11	260	**30**	247	36	675	**74**	694	107
12	1088	**71**	1144	75	1649	91	1729	**78**
13	2209	781	2311	**663**	**2688**	6433	2823	5449
14	3170	**395**	3331	443	3086	**2140**	3263	2364
15	2998	**336**	3188	364	2619	**1253**	2820	1346
16	2237	**201**	2444	210	2578	**473**	2808	503
17	2918	**82**	3163	85	4258	149	4535	**141**
18	5595	**193**	5895	198	7501	**1391**	7831	1510
19	9411	361	9756	**331**	10917	2314	11275	**2166**
20	12424	**426**	12779	435	11451	**2757**	11792	2825
21	10474	**784**	10793	799	8845	**2477**	9131	2526
22	7216	173	7460	**167**	5582	471	5793	**458**
23	3954	**120**	4125	122	-	-	-	-

Table 2

Parameter estimates (median and 95% interval) from four types of interaction models, using weekly central north HFMD data in China 2009–2010.

Parameter	Type I	Type II	Type III	Type IV
α	−1.08 (−1.26, −0.88)	−0.97 (−1.45, −0.48)	−0.84 (−1.31, −0.37)	−0.96 (−1.45, −0.46)
β	0.30 (0.14, 0.45)	0.15 (−0.12, 0.41)	0.33 (0.13, 0.52)	0.16 (−0.11, 0.42)
σ_{γ}	0.15 (0.12, 0.20)	0.17 (0.13, 0.21)	0.15 (0.12, 0.19)	0.15 (0.12, 0.19)
σ_{φ}	0.06 (0.04, 0.09)	0.06 (0.04, 0.09)	0.06 (0.04, 0.09)	0.06 (0.04, 0.09)
σ_{u}	0.13 (0.06, 0.46)	0.19 (0.06, 1.31)	0.13 (0.06, 0.50)	0.24 (0.07, 2.50)
σ_{υ}	0.51(0.43, 0.63)	0.45 (0.36, 0.57)	0.51 (0.42, 0.63)	0.44 (0.35, 0.56)
σ_{b}	4.01(3.87, 4.16)	0.50 (0.47, 0.53)	8.09 (7.78, 8.42)	0.83 (0.79, 0.89)

Table 3

Results of q-weeks ahead prediction using China central north weekly HFMD data from 2009 to 2010. The figures are MSEP, as given by 10 and are for the Type I–IV models, as well as the epidemic/endemic (epi/end) model 11. For each q, figures in bold are the row minimum MSEP.

	$q = 1$					$q = 2$				
$T^\star$	**Type I**	**Type II**	**Type III**	**Type IV**	**Epi/End model**	**Type I**	**Type II**	**Type III**	**Type IV**	**Epi/End model**
90	6204 (0.93)	1563 (0.86)	4758 (1.00)	1421 (0.92)	**1310**	4837	1614	3711	**1488**	2736
91	3129 (0.88)	2492 (0.85)	2704 (0.95)	3263 (0.83)	**873**	2589	5453	2184	7263	**1535**
92	1702 (0.92)	947 (0.81)	1524 (0.97)	**893** (0.85)	3900	2783	1111	2253	**1087**	3093
93	4161 (0.90)	1774 (0.80)	3523 (1.00)	1602 (0.80)	**397**	5255	3051	4510	2774	**583**
94	3576 (0.93)	1071 (0.83)	2993 (0.97)	**984** (0.85)	1670	4495	1909	3768	**1774**	2716
95	5481 (0.86)	**749** (0.83)	4288 (0.97)	755 (0.83)	1655	5693	1834	4755	**1366**	2174
96	5449 (0.88)	2058 (0.73)	5217 (0.98)	2216 (0.76)	**1746**	5321	3352	5468	3789	**1811**
97	5723 (0.88)	1643 (0.76)	4907 (0.97)	1630 (0.78)	**992**	4765	4118	4202	4135	**1268**
98	3940 (0.92)	1757 (0.76)	3569 (0.97)	1813 (0.78)	**836**	3473	2040	3110	2113	**1017**
99	3380 (0.88)	**839** (0.66)	2895 (0.97)	849 (0.71)	927	2590	**955**	2237	971	1621
100	1390 (0.90)	**727** (0.75)	1352 (0.95)	815 (0.76)	1121	1353	**878**	1244	1090	1843
101	853 (0.92)	600 (64)	831 (0.96)	**573** (0.68)	1811	790	602	789	**556**	2106
102	744 (0.88)	**507** (0.69)	729 (0.95)	509 (0.66)	841	773	**529**	756	538	1060
103	924 (0.88)	498 (0.68)	810 (0.90)	512 (0.66)	**302**	-	-	-	-	-

Table 4

Results of cumulative prediction using China central north weekly HFMD data from 2009 to 2010. The figures are MSEP, as given by 10 and are for the Type I–IV models, as well as the epidemic/endemic (epi/end) model 11. For each *q*, figures in bold are row minimum MSEP.

$T^\star$	Type I	Type II	Type III	Type IV	Epi/End model
99	1527	**1852**	1372	1915	3514
100	1695	**1086**	1322	1590	3601
101	784	629	785	**571**	2679
102	773	**529**	756	538	1061
103	924	498	810	512	**302**